CrossMark

ORIGINAL PAPER

Significantly enhanced photocatalytic performance of zinc oxide via bismuth oxybromide hybridization and the mechanism study

Dongfang Zhang[1] · **Fanbin Zeng**[1]

Abstract A highly efficient and stable ZnO–BiOBr composite photocatalyst was prepared by a facile one-pot solvothermal method. A variety of sophisticated techniques such as X-ray diffraction (XRD), X-ray photoemission spectroscopy (XPS), UV–Vis diffuse reflectance spectra, photoluminescence spectra and photoelectrochemical measurement, and so on were employed to characterize the materials. The as-prepared ZnO–BiOBr nanocrystalline showed strong photocatalytic activity for decomposition of methylene blue (MB), Orange II and biphenol A (BPA) under simulated visible light illumination. The possible working principle for the superior photocatalytic properties and reusability of the ZnO–BiOBr hybrid was surveyed to disclose contributions of various effects for the photoactivity enhancement. It was pointed out that *OH and holes take priority over $\cdot O_2^-$ radicals in serving as the main oxidant in the reaction system. The experimental results indicated that the ZnO–BiOBr composite is highly photostable and valuable for real environmental applications.

Keywords Photocatalysis · Nanohybrid materials · Water purification · BiOBr · Stability

✉ Dongfang Zhang
  zjzappletree@163.com

1 College of Science, Huazhong Agricultural University, Wuhan 430070, People's Republic of China

Introduction

Energy crisis and environmental pollution are the two big problems facing the world today [1–5]. On this background, semiconductor-based photocatalyst has draw inflationary number of attention for dealing with environmental pollution and clean energy production. Among them, ZnO is one of the most widely investigated materials due to its abundance, low cost, and little toxicity. Plenty of works [6–8] reported that ZnO shows better photocatalytic activity than TiO2. However, the photocatalytic activity of ZnO is not up to industrial use due to its fast recombination probability of e^-/h^+, lack of visible light absorption, and instability during the course of photocatalytic reaction. These weaknesses restrict the commercialization of ZnO since the development of the efficient photocatalyst is the urgent issue for fixing several environmental problems. In the water field, purification tents to be related to water disinfection for human consumption. Heterogeneous photocatalysis also includes water treatment until stages that not necessarily match the standards for human consumption (purification). Thus, it is indeed challenging to prepare a ZnO-based photocatalyst with a high charge-transfer rate and good separation efficiency of electron–hole pairs.

Semiconductor particle size and its surface properties are two important factors influencing the performance of photocatalysts in that they can influence the separation efficiency of photoinduced electron–hole pairs, besides the photocatalytic oxidation reactions take place at or near the surface. Surface modification benefits the increase in photocatalytic reaction sites, which will improve photocatalytic activity. Compared to TiO2, ZnO holds the flaw of photocorrosion during light irradiation and causes the decline in photoactivity and stability. To

tackle these disadvantages, ample effort has been devoted to hinder the recombination of photogenerated electron–hole pairs and improving the utilization of solar light of ZnO, such as doping, deposition of metals, or combining ZnO with alternative semiconductor [9–11]. It is anticipated that ZnO could become an excellent photocatalyst if the photocorrosion can be suppressed.

As a ternary p-type semiconductor, bismuth oxybromide (BiOBr) with a band gap of 2.73 eV has caused for concern due to its high photocatalytic activity and stability under visible light irradiation [12, 13]. BiOBr possesses a tetragonal matlockite structure, a layered structure with $[Bi_2O_2]^{2+}$ layers interleaved with double Br^- layers. Both the unique open layered structure and emergence of a strong internal static electric field in favor of the effective separation and transfer of photoinduced e^-/h^+, assisting high photocatalytic activity of BiOBr. It has been [14] reported that BiOBr showed high visible light-driven photocatalytic efficiency for a variety of applications including water treatment, disinfection and phenol abatement. Therefore, constructing a firm connection between n-type ZnO and p-type BiOBr can not only widen the light adsorption range of ZnO, but also overcome the shortcomings of BiOBr. However, there is few report deals with the ZnO–BiOBr hybrid catalyst. On this background, the work presented in this case relates to the photocatalytic activity of ZnO–BiOBr composites used for dyes and BPA degradation. The investigation is based on some methods applied for the characterization of the photocatalysts. The given investigation is comprehensive as the photocatalytic mechanism is complete and the use of three reactants for photocatalytic degradation is reasonable.

More specifically, nanoscale ZnO–BiOBr was successfully fabricated by hybridizing of BiOBr with ZnO. The as-prepared ZnO–BiOBr nanocrystalline showed greatly enhanced photocatalytic activity in dye photobleaching assessment. This work has depth in clarifying the photocatalytic nature of the materials for the addressed photodegradation reaction and covers extensive information concerning fundamental mechanism for the creation of radicals. Two issues relate to the i. stability of the prepared specimen and ii. to the reuse possibilities also addressed. The photocatalytic efficiency was tested with few more compounds having different chromophoric groups. The general mechanism behind photodegradation involving electron–hole pair generated via oxidation of dye by the hole or reduction by the electron is well known, and mere disappearance of color does mean that the pollutant is decomposed to smaller organic products essentially. In the case of decolorination of dyes and photocatalytic activity of catalysts, at "Photocatalytic activity" section, the kinetic of decolonization is presented in this work. In the end, the associated

mechanism was put forward to account for the enhanced activity.

Materials and methods

Materials preparation

All chemical reagents utilized were analytical grade reagents purchased from Guoyao Chemical Corporation and used as received. Deionized water was employed in the whole experiment. The synthesis of pure BiOBr or ZnO–BiOBr hybrids was conducted by a one-pot hydrothermal process (Supplementary data in Fig. S1). In a typical synthetic procedure, 0.46 g NaBr and 1.46 g $Bi(NO_3)_3 \cdot 5H_2O$ were dissolved individually in 60 mL 2-methoxyethanol solution under continuous stirring to form solution A and B, respectively. Then, solution A was added drop wise to solution B to form a transparent mixed solution. 0.6 g polyvinyl pyrrolidone (PVP K30) was subsequently added to the mixed solution under vigorous stirring for 30 min, which was transferred to a 100 mL Teflon-lined stainless steel autoclave and maintained at 160 °C for 24 h. After the autoclave was naturally cooled down to room temperature, the resultant precipitates were filtered and washed with deionized water and ethanol for several times to ensure that there is no contamination. Then the as-prepared BiOBr were dried at 80 °C for 5 h to obtain pure BiOBr since the ebullition temperature of ethanol is 78.3 °C. Typical synthesis of ZnO photocatalyst was achieved as follows. In brief, 3 mmol $Zn(NO_3)_2 \cdot 6H_2O$ and 1.5 mmol hexamethylenetetramine ($C_6H_{12}N_4$) were mixed under vigorous stirring. Thereafter, the solution was transferred into a 100-mL Teflon-linked stainless steel autoclave. The autoclave was sealed and heated, in a temperature-controlled oven, at 160 °C for 24 h and then cooled to room temperature naturally. The obtained products were centrifuged, washed, respectively, with absolute ethanol and deionized water three times, and finally dried under vacuum at 70 °C for 5 h to obtain bare ZnO. For comparison, ZnO–BiOBr hybrids were synthesized in the same manner.

Characterization

The phase identification of a crystalline material was identified by X-ray powder diffraction (XRD) technique using Cu K_α ($\lambda = 0.1541$ nm) radiation. The existence of bismuth oxybromide was verified by X-ray photoelectric spectroscopy using a VG MultiLab 2000 system with a monochromatic Mg-Kα source operating at 20 kV. Diffuse reflectance UV–Vis spectra were obtained using a UV–Vis spectrophotometer (Shimadzu 2450 PC) with a barium sulfate-coated integrating sphere inside. Photoluminescence

spectra (PL) were measured at room temperature on a SHI-MADZU RF-5301 PC spectrometer. Photoelectrochemical measurements were taken using a traditional three-electrode cell system based on a CHI 660A instrument. To gain the photoelectrochemical performance of ZnO, BiOBr and BiOBr-hybridized ZnO samples, the dispersed sample in ethanol solution was evenly spread onto ITO (indium tin oxide) glass substrate with a sheet resistance of 15 Ω. After being dried, the ITO glass was calcined for 1 h at 200 °C in N_2 flow. Meanwhile, a platinum electrode and a saturated calomel electrode served as the counter and reference electrode, respectively. The working electrode was irradiated by incident light (400 nm < λ) through a UV-cutoff filter from a 300 W xenon arc lamp. The electrochemical impedance spectroscopy (EIS) was performed from 10^5 to 10^{-2} Hz with an ac voltage amplitude of 10 mV at a dc bias of 0.3 V versus the saturated calomel electrode (SCE) in 0.05 M Na_2SO_4 electrolyte.

Evaluation of photocatalytic activity

The photocatalytic properties of nanophase crystallites were measured via testing the photodegradation rates of dye molecules by various forms, and the samples may show better photocatalytic ability to other dyes, such as cyanine dyes (based on polymethene), and squaraine dyes. The photocatalytic activities were evaluated in terms of decomposition of MB, Orange II and BPA under visible light irradiation. A 300 W xenon lamp equipped with an optical filter (λ > 400 nm) rather than a medium-pressure UV lamp should be used as a light source under this case. The distance between the liquid surface and the light source was about 10 cm. The photocatalyst of 20 mg was dispersed into liquid media containing the model organic components (100 mL, 20 mgL^{-1}) in a beaker by sonication. Herein the used catalyst dosage is not more than 0.5 g/L to make an optimization of the catalysts dose since scattering effects may responsible for reducing degradation extent at high dosage. Then dark experiments were carried out to achieve molecule adsorption equilibrium before light was turn on since MB is a cationic compound and its adsorption onto ZnO occurs better in the alkali media than acidic, due to negatively charged surface of ZnO particles. In the course of photodegradation, 5-mL samples were taken from suspension at given intervals. The filtrates were analyzed by recording variations of the maximum absorption band of a couple of dyes (664 nm for MB and 483 nm for Orange II) using a UV–Vis spectrometer. The remaining percentage of dye was determined by the formula: Removal% = $(C_0 - C)/C_0 \times 100\%$, where C_0 and C represent the initial and residual concentrations of dye. The chemical oxygen demand (COD) of bisphenol A (BPA) or MB solution was measured by a representative chemistry method ($K_2Cr_2O_7$–Ag_2SO_4). Here BPA or MB was chosen as simulated pollutant, as BPA or MB may not be converted to CO2 and water directly without yield complicated intermediates. The removal of COD (W) was calculated according to the following formula: W% = [COD_0–COD_t]/$COD_0 \times 100\%$, where COD_0 and COD_t represent the COD of BPA or MB solution before and after illumination, respectively. All reported data were the average values of three parallel determinations.

Detection of hydroxyl radicals

The active species came into being on the catalyst surface is measured by means of photoluminescence (PL) method using terephthalic acid as indicator, which involving the formation of hydroxyl radical (·OH). The experimental procedures are as follows. The sample was immersed into a 50-mL aqueous solution of 3.0×10^{-4} mol L^{-1} terephthalic acid and 4×10^{-4} mol L^{-1} NaOH in a beaker using the same xenon lamp as the light source. 5 mL of the suspension was withdrawn at definite intervals. PL spectra of the 2-hydroxy terephthalic acid produced were monitored on a Shimadzu RF-5301 PC spectrometer using scanning light wavelength from 350 to 600 nm and excitation wavelength of 310 nm.

Results and discussion

X-ray diffraction and XPS studies

The information about the crystallinity and phase was obtained by X-ray diffraction (XRD), as shown in Fig. 1. It is observed that the diffraction angles at 11.9°, 23.7°,
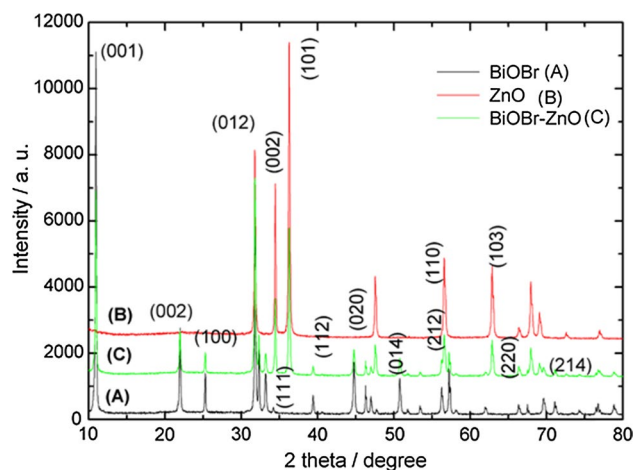

Fig. 1 XRD patterns of the as-prepared **a** BiOBr, **b** ZnO and **c** ZnO–BiOBr samples

26.0°, 32.7°, 39.8°, 44.8°, 48.8°, 54.1°, 58.7°, 68.2° and 76.6° belong to (001), (002), (011), (012), (112), (020), (014), (211), (212), (220) and (310) crystal planes of BiOBr, respectively, which accords with those of pure tetragonal phase BiOBr (JCPDS file Card No. 73-2061). The sharp and narrow diffraction peaks indicated that the sample was well crystallized. Moreover, the diffraction peaks of as-prepared ZnO sample appearing at 31.7°, 34.4°, 36.2°, 47.4°, 56.5°, 62.7°, 66.3°, 67.8° and 69.1° match the crystal plane of a wurtzite structure of ZnO and are comparable to literature values, JCPDS (PDF: #36-1451). No impurity can be detected suggesting that well-crystallized ZnO can be easily obtained under the current synthetic conditions. In the ZnO–BiOBr patterns, diffraction peaks at 11.9°, 23.7°, 26.0°, 32.7°, 39.8° and 44.8°, which can be ascribed to (001), (002), (011), (012), (112) and (020) planes of tetragonal BiOBr, appear. In Fig. 1c, there are two sets of diffraction peaks for the ZnO–BiOBr sample, which are correspondingly ascribed to hexagonal wurtzite ZnO and tetragonal BiOBr, and no peaks of other phases were detected, suggesting that no Bi, Zn-containing impurities exist in the ZnO–BiOBr sample. The patterns of ZnO–BiOBr sample reveal the coexistence of both BiOBr and ZnO phases. Average crystallite size of ZnO–BiOBr composite was estimated according to Scherrer's formula: $d = m\lambda/(b\cos(2\Theta))$, where d was the average grain size (nm), λ was the wavelength of the Cu Kα applied (λ = 0.15406 nm), Θ was the Bragg's angle of diffraction, b was the full width at half maximum intensity of the peak, m is the shape constant of crystal. The average crystallite size of ZnO–BiOBr composite with molar ratio of 1:1 was estimated to be 40.0 nm. The presence of BiOBr was further verified by another manner. The binding energies obtained in the constituent analysis were corrected by referencing the C 1 s line to 284.6 eV. In general, the results are clearly presented with inclusion of XPS spectra, which appears a little disordered in that the intensity differs in each diagram, and in this case we should rather show these spectra as a), b), c), etc. The surveys scan XPS data in Fig. S2 show bromine, oxygen and bismuth elemental peaks for the BiOBr sample, which is consistent with the chemical composition of the photocatalyst. The high-resolution Bi 4f spectrum of the BiOBr sample exhibits two peaks at 159.1 and 164.5 eV, which are characteristic of the bismuth cation of triple valence state in the BiOBr sample. The peak binding energy of 529.9 eV is ascribed to O 1 s. Meanwhile, the peak located at 68.3 eV is assigned to Br 3d. This is typical characteristic of the bromine anion of single valence state in the BiOBr sample.

Optical properties

The optical absorption properties play a critical role in determining the photocatalytic activity of a catalyst. The spectra can be used to find out the type of electronic
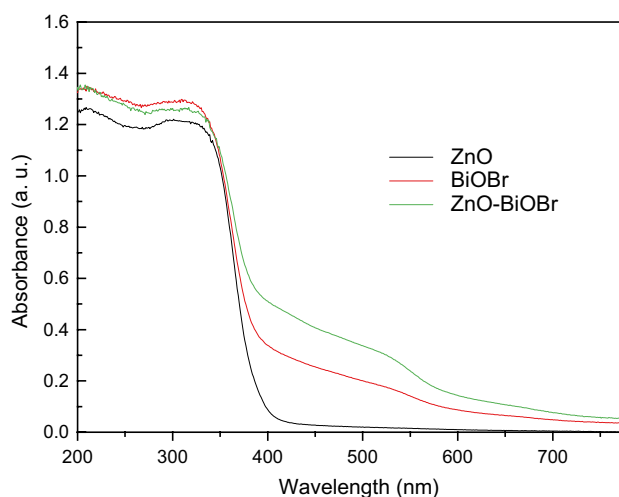

Fig. 2 UV–Vis diffuse reflectance spectra of the as-prepared ZnO, BiOBr and ZnO–BiOBr samples

transition and the band gap of the composites allowing to make some conclusions in the photocatalytic mechanism part. Figure 2 shows the UV–Vis diffuse reflectance spectra of the as-prepared ZnO, BiOBr and ZnO–BiOBr samples. The vertical axis of the optical absorption spectra is not in an arbitrary unit to make it is possible to compare absorption intensities between samples. It was found that ZnO had an absorption edge around 395 nm and exhibited relatively strong absorption in the UV region. By comparison, the UV–Vis DRS spectra show that the BiOBr and ZnO–BiOBr composite photocatalysts exhibited stronger absorption in visible light range than bare ZnO. This can be ascribed to that the electron transitions from antibonding states of majority O2p and minority Bi 6 s character at the top of the valence band [15]. Moreover, the absorption intensity in the visible light range is improved for ZnO–BiOBr composite. These observations suggest an increase in surface electric charge in the composite due to BiOBr hybridization, which may lead to modifications of the fundamental process of electron–hole pair formation. Therefore, comparing with pristine ZnO, BiOBr and BiOBr–ZnO composites can be excited to generate more e^- and h^+, resulting in a high potential ability for photodecomposition of organic contaminants rapidly. It is believed that these catalysts will show photocatalytic activity in the order BiOBr–ZnO > BiOBr > ZnO. Thereby, this study could provide one with a new way of increasing selectivity for a desired sequence of products since there be a way to obtain numerical band gap measurements for different compositions. During a photocatalytic stage, creation of photoinduced electron population in the conduction band always creates room for e^-/h^+ encounter. Namely, the effective photocatalytic activity depends on successful prevention of e^-/h^+ recombination.

It is now commonly recognized that, among the many factors, the number of photogenerated charge carriers plays an important role in affecting the photocatalytic performance: The higher the number of carriers, the better the photocatalyst. In this work, we attempted to explain BiOBr–ZnO possesses the best photocatalytic performance. The photoinduced charge separation rate is proposed to be characterized by photoluminescence (PL) emission spectra or surface photovoltage spectroscopy, it will help with results discussion. It is known that lifetime of the photoproduced electron–hole pairs plays an indispensable role in affecting the photocatalytic performance. Photoluminescence (PL) spectroscopy is a valuable tool for investigating the fate of electron–hole pairs, and fluorescence intensity is an important basis for evaluation of the carrier's movement. In addition to the recombination of free carriers, the intensity is dependent on the sample loading used in the measurements. So, the amount of materials was set the same to make it easy to compare the differences in fluorescence intensities among these samples. The life span of photoinduced e^-/h^+ is given in Fig. 3. All the samples show similar pattern with broad shoulders between 300 nm and 500 nm. The observed PL cannot be ascribed to direct exciton recombination as it involves trap states. The differences between blue PL observed here and typical green PL can be related to different depth of trap states. Maybe more structural defects are present after the coupling process which quenches the high-energy emission by lower lying states, etc. This broad green emission can be assigned to the charge carrier relaxation via surface-related trap states such as oxygen vacancies on the substrate. This emission peaks in the blue-green band might originate from the shift of the ionized oxygen vacancies to the valence band [16]. It is drawn that the higher the oxygen vacancy and defect content is, the stronger the PL signal is. Moreover, oxygen vacancies can facilitate the adsorbed O_2 to capture photoinduced electrons, simultaneously producing $\cdot O_2^-$ radical groups. Thus, it can be deduced that oxygen vacancies and defects are in favor of photocatalytic reaction. In theory, excitonic PL signals attribute to self-trapped excitons, V_O (an oxygen-ion vacancy occupied by two electron) and V_O^+ (an oxygen-ion vacancy occupied by one-electron centers), respectively. There were lots of oxygen vacancies on the surface of host nanocrystals [17], and nanocrystalline size was fine so that the average distance the electrons could move freely was very short. These factors could make the oxygen vacancies bind electrons easily. Thus, the exciton energy level near the bottom of the conduction band could come into being, and the PL band of the excitons could occur, meanwhile leading to drop in recombination chance of photogenerated charge carriers, consequently promoting charge separation and transfer. The excitonic emission intensity of ZnO–BiOBr, BiOBr
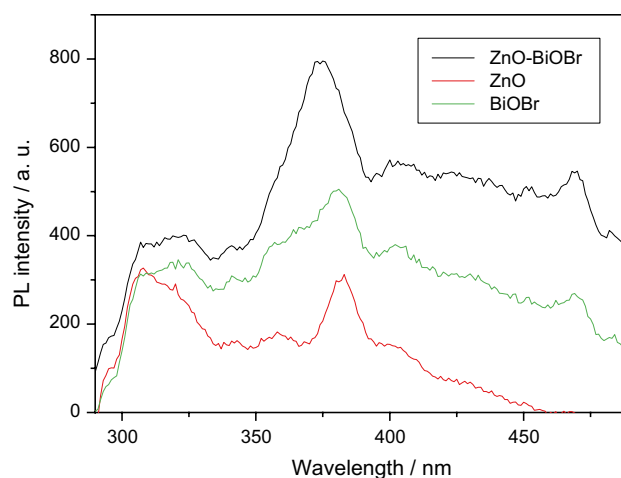

Fig. 3 Photoluminescence spectra of the as-prepared ZnO, BiOBr and ZnO–BiOBr samples

and ZnO gets weaker in order, indicating that the content of surface oxygen vacancy and defect is in the order of ZnO < BiOBr < ZnO–BiOBr. It was concluded that ZnO–BiOBr composite has better photocatalytic capability than bare BiOBr or ZnO. Oxygen vacancies and defects can become centers to capture photoinduced electrons, so that the recombination of e^-/h^+ can be effectively inhibited [18]. Moreover, oxygen vacancies boost the adsorption of O_2 on crystal facets. The adsorbed O_2 accept e^- and form $\cdot O_2^-$, which leads to the formation of active $\cdot OH$ promoting the oxidation of organic substances [19]. It is true that the visible PL peak is related to the number of defects (not just oxygen vacancies, however), and it is clearly established that the intensity of the UV (i.e., excitionic) PL peak is inversely proportional to defects. To conclude, oxygen vacancies and defects are beneficial to photocatalytic activity since the efficient charge separation can lengthen the lifetime of charge carriers. It is stated that the optical property is one of the reasons affecting photocatalytic property but not the major factor. The association of photoluminescence mechanism with photooxidation ability is very complex, and a detailed study is needed.

Photoelectrochemical measurements

Photoelectrochemical experiments were performed to solve the electronic interaction between ZnO and BiOBr. It can be used to determine the flat-band potential as well as band gap and create the energy diagram for the photocatalytic mechanism section. The transient photocurrent responses of different electrodes can be recorded via several on–off cycles of irradiation. Figure S3 depicts the photocurrent transient responses. For each sample, an anodic photocurrent peak, which decayed rapidly

followed by a steady current, appears at the initial time of irradiation. When the light is interrupted, the holes accumulated in the surface state still continue to recombine, and a cathodic peak is observed. It is discernible that each sample was prompt in generating photocurrent with a reproducible response to on–off cycles, demonstrating the effective charge transfer and successful electron collection. Since ZnO almost not be activated by visible light illumination ($\lambda > 400$ nm), the corresponding photocurrent for ZnO/ITO electrode is close to zero. In comparison with pure BiOBr, ZnO–BiOBr mixed crystal exhibited an increased photocurrent density. The photocurrent density of the ZnO–BiOBr /ITO is greater than 0.93 mA cm^{-2}, whereas that of BiOBr/ITO is only 0.17 mA cm^{-2}. The photocurrent of the ZnO–BiOBr is about six times as great as that of BiOBr solely. The photocurrent improvement indicated a higher separation efficiency of photoinduced electron and holes, which attributes to the interaction between BiOBr and ZnO. As a result, the recombination of photogenerated charge carriers was suppressed. The separation and transfer of electron and hole pairs was identified using electrochemical impedance spectroscopy (EIS) [20]. The radius of the arc on the EIS Nyquist plot reflects the reaction rate occurring at the surface of electrode. The smaller the radius of the EIS Nyquist plot, the lower the electric charge-transfer resistance is. The results indicate that more effective separation of photogenerated e$^-$/h$^+$ and faster interfacial charge-transfer occurred in the case of BiOBr-hybridized ZnO electrode, whereas ZnO/ITO electrode cannot respond to visible light illumination. Only one arc/semicircle is observed in Fig. 4, implying that only the surface charge-transfer step is in the photocatalytic reaction. The radius of the arc on the EIS Nyquist plot reflects the reaction rate occurring at the surface of the electrode. As can be seen, the arc radius of the ZnO–BiOBr/ITO is smaller than that of the BiOBr/ITO under visible light irradiation, indicating a fast interfacial charge transfer to the electrode donor/electron acceptor and an effective separation of photogenerated electron–hole pairs as suggested [21], which would contribute more significantly to the remarkable enhancement of photocatalytic activity.

Photocatalytic activity

Testing a material as a visible photocatalyst using dye as model substrate is an option to look the science behind the photocatalytic behaviors. The dye has an absorption band in UV and visible region affecting the photoexcitation on the photocatalyst. Moreover, the decoloration of the dye including oxidation and reduction processes is complicated and not simply associated with the photoinduced decomposition. The photoactivity was explored by
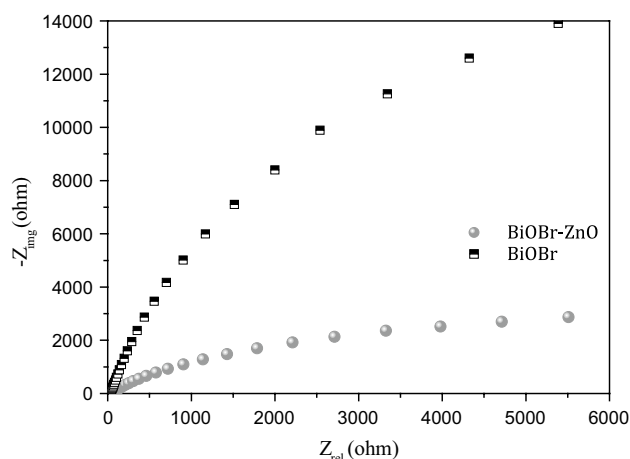

Fig. 4 EIS Nyquist plots of the as-prepared BiOBr and ZnO–BiOBr samples under visible light irradiation

the degradation of MB, while methylene blue (MB) often occurred in wastewater and caused serious environment problems because it was chemically stable and biologically less active. Besides, MB is refractory, to some extent, based on N-alkyl groups. Thus, the photodegradation of MB was chosen to investigate the photocatalytic activity (>400 nm) of the BiOBr/ZnO composite in comparison with the pure BiOBr and ZnO, and the result is shown in Fig. 5. To effectively demonstrate the photocatalytic activity of samples, C/C_0 or $(C_0-C)/C_0$ versus reaction time should be plotted. Photolysis tests should also be carried out as a control experiment including the dark adsorption results. Control experiment results implied that the MB degradation performance can be ignored in the absence of either irradiation or photocatalyst, indicating that MB was degraded via photocatalytic process. Thus, the result indicates self-photodegradation of MB or dye-photosensitization is almost negligible in the current situation. Also adsorption of the organic substrate is not a crucial process. Generation of reactive oxygen species, usually responsible for the pollutant degradation, does not require adsorption of the organic molecule, and this issue will be discussed later. The stability of the catalyst also needs to be investigated in this study. The photocatalytic efficiency of MB over the above samples for such kind of experiments is shown in Fig. 5a. A blank experiment with the reference photocatalyst (pure ZnO) is also vital since the absorbance of pure ZnO is small but could be enough to effectively degrade the employed dyes. It should be noted that the adsorption phenomena during light experiments are going to be totally different than those during dark experiments. In fact, light is leading to a particular type of active sites promoting adsorption and degradation of organic molecules. The control experiment indicates self-photodegradation of MB or dye-photosensitization is almost negligible in the current situation, whereas
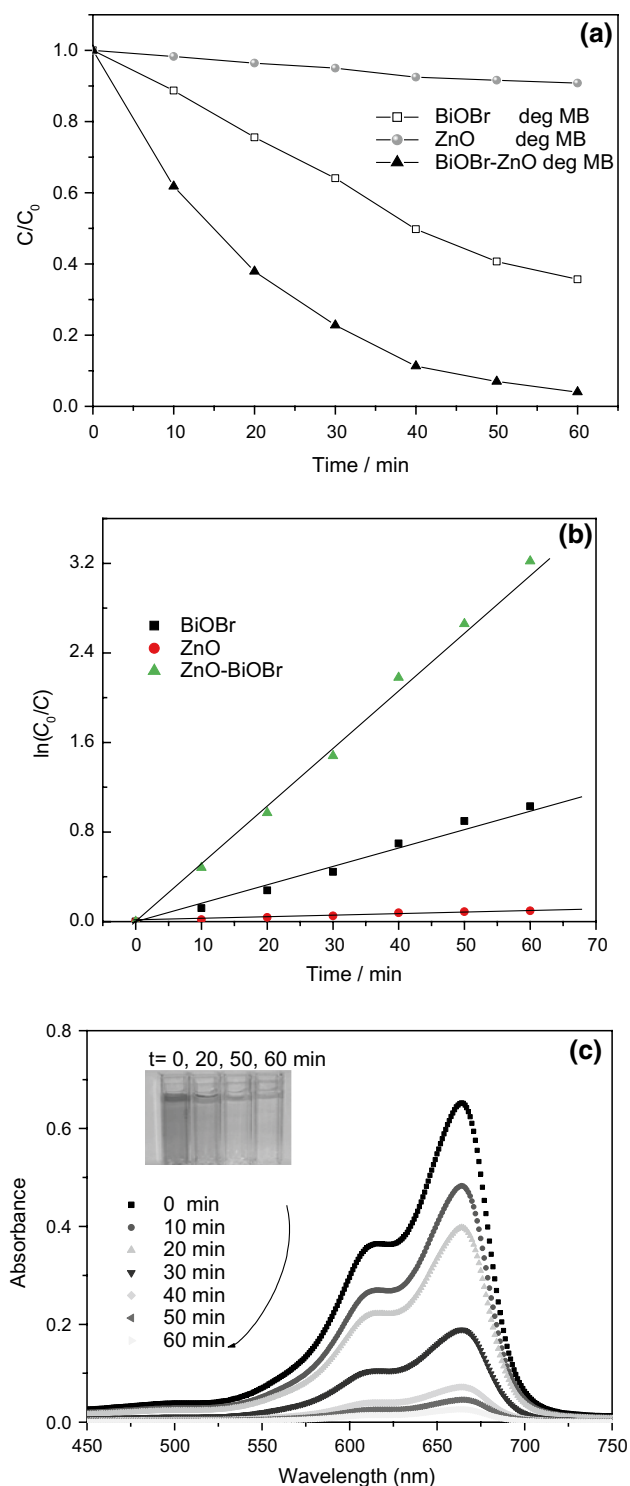
Fig. 5 Reaction process for photocatalytic degradation of MB **a** with different catalysts under simulated visible light irradiation ($\lambda > 400$ nm), **b** variation in $\ln(C_0/C)$ as well as linear fit as a function of photolysis time and **c** temporal spectral traces during the course of the photodegradation of MB with ZnO–BiOBr composite

the hybrid catalyst displays high photocatalytic activity, as almost 68 and 96% of MB was degraded for only 60 min, respectively. The results hint that the composite exhibits, however, much faster decomposition rate compared to BiOBr or ZnO. That is, during 60-min photocatalysis the ZnO–BiOBr composite was able to completely bleach MB dye, while BiOBr and ZnO only resulted in a partial and negligible decomposition, respectively. It is desirable to make a quantitative assessment of MB discoloration. For purposes of comparison, the decrease in the dye concentration should be given as a function of time so that the degradation kinetics can be evaluated and it is easy to tell how much of the dye was removed. The quantitative assessment should be done comparing the pseudo-first-order kinetics of "discoloration," mediated by both photocatalysts. Therefore, the kinetic behaviors of photocatalytic decomposition of MB treated with pure ZnO, bare BiOBr and ZnO–BiOBr composite under simulated light source were explored by using Langmuir–Hinshelwood model, given as: $\ln(C_0/C) = kt$, where 'C' is the dye concentration at fixed time 't,' 'C_0' is the initial concentration of the dye solution, and 'k' is the pseudo-first-order rate constant. Of course, there is no need to argue with the Langmuir–Hinshelwood mechanism when the experimental result is a simple exponential decay (first-order kinetics). The linear plot between $\ln(C_0/C)$ and time (t) of light exposure for all the catalysts of pure ZnO, bare BiOBr and ZnO–BiOBr composite is shown in Fig. 5b. In addition to the removal% of the dye color, the constant rate of the process has been determined and it follows a pseudo-first-order mechanism. The degradation rate constant (k), estimated from the slope of $\ln(C_0/C)$ verses 't' curve, was three folds higher for ZnO–BiOBr composite ($k = 0.054$ min^{-1}) than pure BiOBr ($k = 0.0172$ min^{-1}) and far beyond than that of bare ZnO ($k = 0.0016$ min^{-1}) based on kinetic theories for catalytic reactions.

In order to complete the photocatalytic experience of MB with ZnO–BiOBr composite, the degradation profiles (Fig. 5c) were given to provide information on changes in absorption maxima with time. According to the literature, deethylation and chromophore cleavage are analogous competitive photodegradation reactions during the photocatalytic decomposition of organic pollutants [22]. It could be seen that the characteristic absorption around 664 nm decreased with the increase in irradiation time. However, the maximum absorbance exhibits slight hypsochromic shift. Therefore, we can infer that the chromophore cleavage of MB structure predominates upon ZnO–BiOBr composite, and the way of MB degradation reaction does not change since no absorption peaks due to intermediate products of MB molecules can be found, which may

be indicative of full decomposition. The results demonstrate that bleach of target dye happens irreversible during photocatalysis. In addition, degradation phenomenon toward model pollutant with different chromophores such as Orange II was also tested and is given in Fig. 6a. The falling down in the absorption peak in the range of 200–300 nm proving the absence of benzene derivatives at the end of photodegradation process. The stability and long-term efficacy of photocatalysts are also important factors for practical applications. Stability test issue or quantitative information on the time dependence of the photocatalytic effects is urgently needed. Therefore, cycle treatments were carried out to track the catalyst stability. We try to repeat the experiments to see whether the preparation methods and results are reproducible (preferably triplicated), and Orange II degradation is perhaps a good choice.

As depicted in Fig. 6b, the photocatalytic activity of ZnO–BiOBr with error bar needed for the data shows no evident loss after three cycles, indicating the high photocatalytic stability during the reaction course. The error bars in the graph imply that the experiments were done not only once, which is sufficient to conclusively demonstrate an effect. The photocatalytic activity of ZnO–BiOBr composite still reached 85%, even though it had been used 3 times repeatedly. This indicates that ZnO–BiOBr composite can remain stable and keep efficient activity, which makes it a potential photocatalyst for environmental remediation of contaminated drinking water resources.

Photocatalytic mechanism

It is already accepted that lots of reactive oxygen species (ROSs) including h^+, $\cdot OH$ and $\cdot O_2^-$ perhaps involved in photocatalytic oxidation process [23, 24]. Therefore, radical and hole trapping experiments were undertaken to verify the existence of oxidative species and to reveal the internal mechanism as the intermediate products were simply overlooked by UV–Vis analysis. The effects of different scavengers on photocatalytic performance can be investigated. The typical scavengers are ammonium oxalate for h^+, isopropanol for $\cdot OH$ and benzoquinone for $\cdot O_2^-$; in this way the photoinduced charge separation rate can be speculated to some extent. The hole can oxidize the adsorb H_2O or OH group to form OH radical, and the electron can react with O_2 to produce the superoxide. Reaction intermediates formed by OH radical attack and other reactive oxygen species on specific sites of the target contaminants may appear. To determine the formation of active radical species (e.g., $\cdot OH$, $\cdot O_2^-$, H_2O_2), the quenching effects of the selected scavengers should be supplemented. Formic acid (HCOOH), sodium azide (NaN$_3$), isopropanol (IPA) and potassium iodide (KI) could be used as scavenging species to investigate the generation and roles of $\cdot O_2^-$, $^1O_2$,
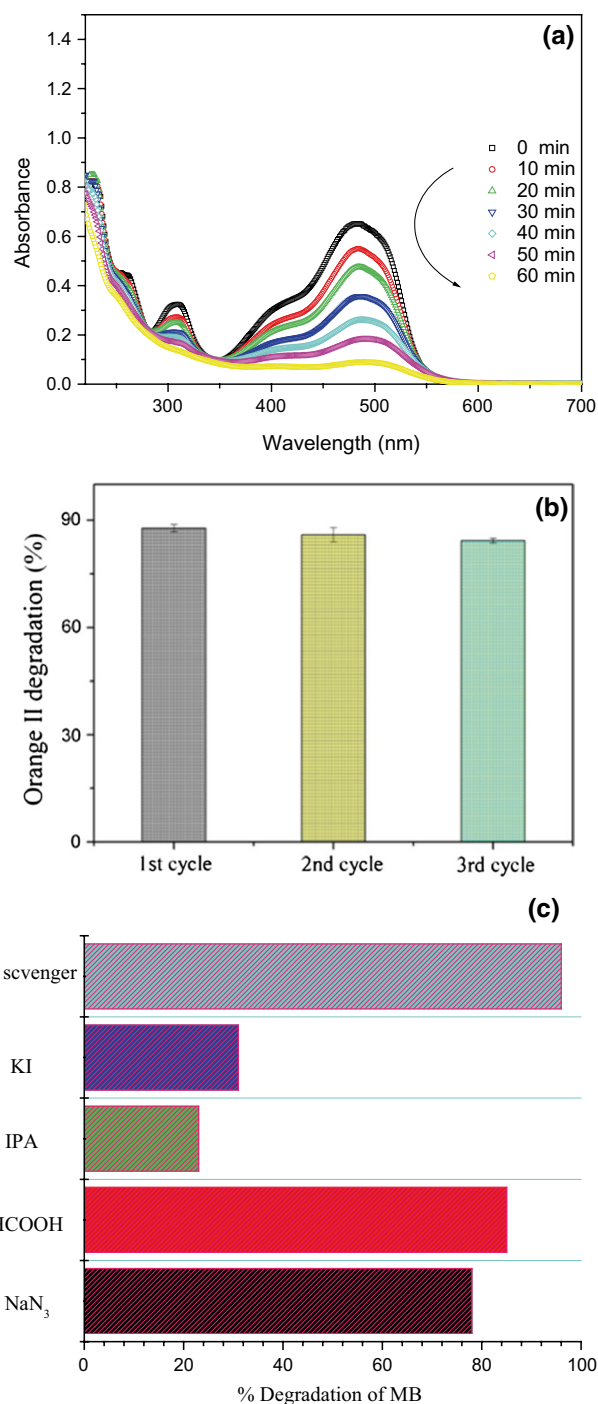

Fig. 6 Absorption spectra of Orange II solution **a** in the presence of ZnO–BiOBr composite photocatalyst under simulated visible light irradiation ($\lambda > 400$ nm), **b** cycling runs of the ZnO–BiOBr composite in the photodegradation of Orange II and **c** the extent of degradation of MB using ZnO–BiOBr catalyst with and without scavengers

$\cdot OH$ and h^+, respectively. In the present study, 0.2 mM of HCOOH, NaN$_3$, IPA and KI were added as scavengers on the degradation of MB in attempt to elucidate the underlying mechanism. MB dye is picked up since the dye

sensitization under visible light could be omitted totally and MB was deemed as azo dye (based on –N=N– structure) that is difficult to break down. As shown in Fig. 6c, compared to without any scavenger on this occasion, the photocatalytic activity in ZnO–BiOBr heterogeneous catalytic system is greatly suppressed by the addition of IPA (*OH radical scavenger) and KI (hole scavenger), indicating the main roles of *OH and h$^+$ for MB degradation. The addition of HCOOH which acting as a sacrificial electron donor (·O$_2^-$ radical scavenger) and NaN$_3$ (^{1}O$_2$ scavenger) exerted only a feeble influence in PCO process of MB, suggesting that ·O$_2^-$ and ^{1}O$_2$ played comparatively minor role for MB degradation. It is clear that the degradation of MB was restrained in the presence of these scavengers with the order of significance following IPA > KI > HCOOH > NaN$_3$. Thus, it is postulated that *OH followed by h$^+$ significantly contributed to the degradation of MB, while the roles of ·O$_2^-$ and ^{1}O$_2$ were less significant. On the basis of the experimental observations, a tentative mechanism for photocatalytic degradation of dye may be proposed as below. Dissolved oxygen reacts with the electron located in the conduction band of semiconductor forming oxygen radical anion. This radical anion reacts with proton forming hydrogen peroxide radical, which in turn will oxidize the dye to its leuco form. This leuco form ultimately degrades to the products. Also ·O$_2^-$ radicals formed in situ during the reaction, leading to termination of the chain reaction to successfully produce hydroxyl radicals. Thus, it was confirmed that *OH radical does act as main oxidizing species, as the reaction rate greatly affected in the presence of *OH radical scavenger, isopropanol. It once claimed by the previous work that fluorescence spectra cannot totally confirm the separation efficiency of carriers, and detecting hydroxyl radicals using terephthalic acid as a probe molecule can be executed. Regarding this, photoluminescence (PL) data should be provided since *OH was speculated as the predominant active species that participate in the reaction.

In order to ascertain the existence of *OH, radicals formed on photoilluminated ZnO–BiOBr surface were checked and the outcome are expressed in Fig. 7. It can be seen that ZnO–BiOBr can produce *OH after illumination and the fluorescence intensity of PL signal at 425 nm increases along with irradiation time. This suggests that the fluorescence is caused by chemical reactions of TA with *OH formed in ZnO–BiOBr system, while the fluorescence intensity was proportional to the amount of *OH produced [25]. Hence, *OH is the reactive oxygen species to get rid of MO straightforward. Generally, two competitive processes, charge carriers recombination versus interfacial charge transfer, may occur after the creation of photogenerated charge carriers. The former eliminated the photogenerated electrons and holes, while the latter produced active radical species (e.g., *OH, ·O$_2^-$, H$_2$O$_2$).
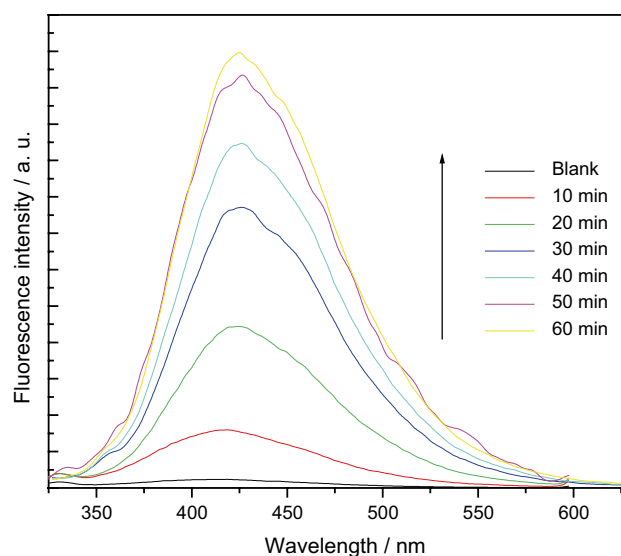

Fig. 7 Change of fluorescence spectrum with addition of ZnO–BiOBr composite in 3.0×10^{-4} M basic solution of terephthalic acid

Besides, the band levels of the ZnO–BiOBr composite should be described with the aim of explaining the proper mechanism. Thus, the band structures of this material should be confirmed by theoretical calculations. The flat-band potential of BiOBr was calculated using the Mulliken electronegativity rule: $E_{VB} = \chi(A_aB_bC_c) + E_0 + 0.5E_g$, $E_{CB} = E_{VB} - E_g$, where E_{VB} is the top potential of valance band, E_{CB} is the CB bottom potential, E_g is the band gap energy of BiOBr, and E_0 is the scale factor taken as -4.50 eV, i.e., the energy of free electrons on the normal hydrogen electrode (NHE scale). The parameter $\chi(A_aB_bC_c)$ corresponds to the absolute electronegativity of a semiconductor material type $A_aB_bC_c$ such as BiOBr, which is calculated as the geometric mean of the electronegativity of the constituent atoms. Based on the above analysis, the band edge potentials of the CB and VB of BiOBr were speculated to be 0.27 and 3.19 eV, respectively, whereas those for ZnO are -0.29 and 2.91 eV, respectively [26]. A more positive VB top is known to correspond to stronger oxidation ability, and a more negative CB bottom corresponds to stronger reduction ability. The CB potential of BiOBr (0.27 eV) is less negative than the standard reduction potential of oxygen (-0.046 eV) [27], suggesting that E_{CB} on the BiOBr surface cannot deoxidize O$_2$ into ·O$_2^-$, whereas ZnO can deoxidize O$_2$ into ·O$_2^-$. However, the VB potential of BiOBr (3.19 eV) was more positive than that of ZnO, indicating that BiOBr owned higher oxidation ability. Under visible light irradiation ($\lambda > 400$ nm) photogenerated electron–hole pairs emerge from the photoexcited BiOBr. Then some of the photogenerated holes accumulated in BiOBr could interact with surface-bound H$_2$O or OH$^-$ to produce the ·OH species. Because of the lower conduction

band edge potential of BiOBr (0.27 eV), the photoinduced electrons could not provide a sufficient potential to reduce O_2 to $\cdot O_2^-$ through the one-electron reduction process and further generate *OH. Dye such as MB^* renders an e^- to become a cation MB^+ and then decays after reaction with $\cdot O_2^-$ leading to disappear of MB immediately. In the presence of light and vapor (H_2O), the radicals *OH and $\cdot HO_2$ are produced besides H_2O_2 that in solution to discolored MB. Additionally, when electrons are excited from the visible light responsive BiOBr catalysts, most of the holes from the valence band (VB) of BiOBr will automatically drifted to the VB of ZnO from the thermodynamic consideration, and thereby the e^-/h^+ recombination was retarded. That is, the synergetic effect existed in the ZnO–BiOBr nanocomposite, resulting in the enhancement of charge separation in the photocarriers generation process happened at the interface, and a lot of holes will be captured to promote photocatalytic reactions ultimately [28–35]. The improvement of the photocatalytic efficiency due to the electron trap effect played by the cooperative effect is beneficial [36–43]. In addition, the energy levels of O_2/H_2O_2 (0.68 V vs NHE), $HO_2\cdot/H_2O_2$ (1.50 V vs NHE) and H_2O/H_2O_2 (1.80 V vs NHE) are also located within the band gap of ZnO, indicating that H_2O_2 generation by photoexcited electron is feasible and can stimulate photocatalytic processes. The energy levels of the redox couples leading to generation of respective reactive oxygen species, e.g., H_2O_2 and *OH for photodestruction of organics [44–46]. To conclude, the present results reveal that the as-prepared ZnO–BiOBr composite can be used as a prospective candidate as a photocatalyst for remedy color dyes and all other chemical pollutants such as pesticides, toxins, and pharmaceuticals in the wastewater.

The photocatalytic degradation is followed and evaluated mainly by monitoring the UV–Vis spectra of the tested solution. The shortcoming of this method is that it cannot reflect the total mineralization of the substrates used here. In general, the disappearance of color of dye with time does not indicate destruction of the dye molecule directly although the results of blank experiments lead to the minor possibility of the self-photosensitized pathway by dyes used in our situation. When using visible light, it is always better to use a molecule, which does not interact with the radiation, like 4-chloro phenol, dichloro acetic acid, and formic acid. The fact that the dye does not undergo photodegradation in aqueous solution (in the absence of catalyst) does not guarantee that it is unable to absorb visible light and inject electrons in the semiconductor conduction band, once it is adsorbed on the semiconductor itself, i.e., a self-sensitized photodegradation mechanism cannot be excluded at all. The photocatalytic activity of the prepared catalyst can be convincingly assessed using colorless pollutants as the

probe molecules since dyes tend to be photochemically decomposed under vis radiation. A non-absorbing degradation substrate should be chosen to demonstrate that the as-prepared photocatalytic materials exhibit indeed activity under visible light. Therefore, additional test such as COD analysis is needed for approved mineralization of degradation products. The COD levels in the reaction solution can be employed to demonstrate the presence of intermediates organics in solution. The COD removal efficiency of substrate degraded with reaction time using as-prepared catalysts was determined. An appropriate substrate can be used for the evaluation of photocatalytic reaction, which usually refers to a colorless pollutant such as bisphenol A (BPA). In order to further evaluate the photocatalytic performance, the removal of COD for MB and BPA after 1.0 h irradiation was investigated and is shown in Fig. 8. It was found that the COD removal efficiency by using BiOBr or BiOBr–ZnO sample was 46.0–79.0% after 60 min. It is easy to found that the COD removal efficiency for MB removal was lower than the corresponding degradation efficiency (by ca. 20%) within the studied reaction period. These results further indicated that MB dye was oxidized via a number of intermediates prior to its final product of CO_2. As is depicted, the removal efficiency of COD for BPA or MB was increased in the presence of these catalysts with the order following BiOBr–ZnO > BiOBr > ZnO. The efficiency of COD removal was strongly affected for coupling of BiOBr with ZnO component, whereas the COD removal rates were similar to degradation of bisphenol A or MB by BiOBr–ZnO hybrid alone. The result confirms the superior photocatalytic properties of ZnO–BiOBr heterostructure than single BiOBr or pure ZnO, and bisphenol A or MB can be effectively decomposed to smaller organic molecules such as carbonate, CO_2 and other harmless or less harmful inorganics at last. These quantitative results
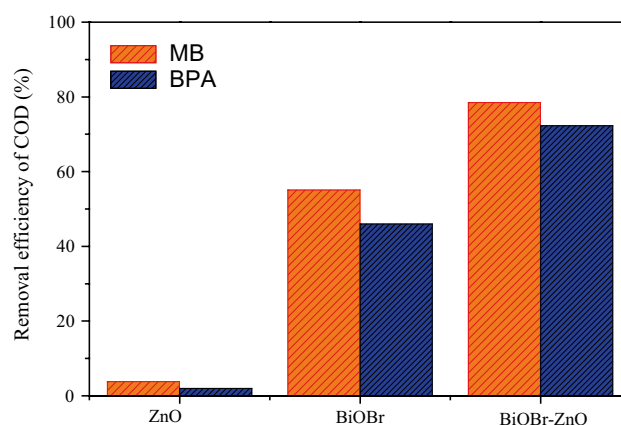

Fig. 8 COD removal of BPA and MB photolyzed over as-prepared ZnO, BiOBr and ZnO–BiOBr photocatalysts under simulated visible light irradiation ($\lambda > 400$ nm) for 1.0 h

Table 1 Comparison on the degradation of azo-dyes (MO, MB or RhB) using BiOX (X = Br, Cl)-based photocatalysts

Material	Preparation method	$C_{catalyst}$ ($\times 10^3$ mg/L)	Light source	Rate constant k ($\times 10^{-3}$, min^{-1}) of substrate degraded	Refs.
BiOBr	Solvothermal synthesis process	0.5	500 W xenon lamp (light intensity = 600 mW/cm^2, λ > 420 nm)	RhB dye: 15.6–77.1	[47]
g-C$_3$N$_4$/BiOCl	Ultrasonic-assisted hydro-thermal process	1.0	500 W xenon lamp (light intensity = 50 mW/cm^2, λ > 420 nm)	MB dye: 5.1–6.6	[48]
Ag–BiOCl	One-pot nonaqueous approach	1.0	Xenon arc lamp (λ ≥ 420 nm), 500 W	MO dye: 4.6–20.9	[49]
BiOBr	Solvothermal method	0.5	300 W xenon lamp (λ > 400 nm)	RhB dye: 53.9	[50]
BiOBr/CeO$_2$	Solvothermal method	1.0	Visible light irradiation: 300 W Xe lamp	RhB dye: 67.0	[51]
BiOBr–ZnO	Solvothermal method	1.0	UV–Vis light source: 500 W xenon lamp	MO dye: 9.3–43.3	[52]
Bi$_2$S$_3$/BiOBr	One-pot solvothermal method	1.0	150–350 W xenon lamp (λ > 420 nm)	RhB dye: 48.9	[53]
BiOBr	Hydrolysis process	1.0	500 W xenon lamp (λ ≥ 400 nm)	MB dye: 4.2	[54]
BiOBr–ZnO	One-pot hydrothermal process	0.2	300 W xenon lamp equipped with an optical filter (λ > 400 nm)	MB dye: 54.0	Present study

implied that the incorporation of n-type ZnO component into p-type BiOBr to form a novel p–n heterostructure endows BiOBr-ZnO composite with positive response to the visible light, and this property was not affected by the introduction of ZnO component in the photocatalyst. Moreover, a comparing is needed for the results of this work with other similar photocatalysts in spite of advantages of newly introduced photocatalyst. The photocatalytic performance of the materials developed in this study was compared with those reported in the literature, targeting on the degradation of typical azo-dyes such as methyl orange (MO), methylene blue (MB) or rhodamine B (RhB) in water using BiOX (X = Br, Cl)-based photocatalysts (Table 1). Whereas the rate constants (k values) varied depending on the preparation of materials and the experimental setups, it was obvious that the BiOBr-ZnO composite photocatalyst exhibited a higher k than pure BiOBr, and comparable to the g-C$_3$N$_4$/BiOCl, Ag–BiOCl, BiOBr/CeO$_2$ and Bi$_2$S$_3$/BiOBr photocatalysts [47–54]. It was worthwhile to mention that the concentration of photocatalyst in MB solution in the current study was 200 mg/L, much lower than those reported by others (0.5–1.0 g/L). Considering this factor, the photocatalyst developed in this study had a unique advantage of maximizing the photocatalytic performance efficiently and effectively, and the p–n heterostructure comprising p-type BiOBr and n-type ZnO that constructed offers the material to be easily recycled and reused. It could be a promising strategy for designing new efficient photocatalysts for application in eliminating organic pollutants from wastewater.

Conclusions

In summary, this study demonstrates a clean, nontoxic and environment friendly synthetic strategy for the preparation a highly efficient and stable ZnO–BiOBr hybrid photocatalyst. The resultant ZnO–BiOBr nonmaterial was used as an environmentally benign catalyst, which showed high solar light photocatalytic activity and can be used in practice. The maximal degradation efficiency of MB in aqueous solution has reached 96% after irradiation for 60 min. It was found that the ZnO–BiOBr hybrid can be reused several times without any loss in activity. After three cycles of repetition tests, the degradation efficiency and structural stability were remain efficient and stable. Radical capture investigations justify that the degradation of MB over ZnO–BiOBr is mainly via *OH and h$^+$ oxidation mechanism. This study provided a potential approach to the removal of hazardous pollutants under sunlight, which using ZnO–BiOBr as an ideal candidate. In addition, this work inspires the exploration of similar approaches to stabilize easily photocorroded photocatalysts. The materials and processes being costless, time effective and can be applied for cleaning of contaminated water bodies.

References

1. Z.Z. Yuan, X.X. Zhu, M.R. Li, W.J. Lu, X.F. Li, H.M. Zhang, Angew. Chem. Int. Ed. **55**, 3058 (2016)
2. Z.Z. Yuan, Y.Q. Duan, H.Z. Zhang, X.F. Li, H.M. Zhang, I. Vankelecom, Energy Environ. Sci. **9**, 441 (2016)
3. H.Z. Zhang, H.M. Zhang, F.X. Zhang, X.F. Li, Y. Li, I. Vankelecom, Energy Environ. Sci. **6**, 776 (2013)
4. H.Z. Zhang, H.M. Zhang, X.F. Li, Z.S. Mai, W.P. Wei, Energy Environ. Sci. **5**, 6299 (2012)
5. H. Jin, H.M. Zhang, H.X. Zhong, J.L. Zhang, Energy Environ. Sci. **4**, 3389 (2011)
6. S.G. Kumar, K.S.R.K. Rao, RSC Adv. **5**, 3306 (2015)
7. A. Omidi, A.H. Yangjeh, J. Iran. Chem. Soc. **11**, 457 (2014)
8. H. Zhang, R. Zong, Y. Zhu, J. Phys. Chem. C **113**, 4605 (2009)
9. M. Esmaili, A.H. Yangjeh, J. Iran. Chem. Soc. **7**, S70 (2010)
10. M. Movahedi, A.R. Mahjoub, S.J. Darzi, J. Iran. Chem. Soc. **6**, 570 (2009)
11. J.L. Zhang, Y.M. Wu, M.Y. Xing, S.A.K. Leghari, S. Sajjad, Energy Environ. Sci. **3**, 715 (2010)
12. J. Li, Y. Yu, L.Z. Zhang, Nanoscale. **6**, 8473 (2014)
13. X.Y. Xiao, J. Jiang, L.Z. Zhang, Appl. Catal. B Environ. **142–143**, 487 (2013)
14. X. Zhang, Z.H. Ai, F.L. Jia, L.Z. Zhang, J. Phys. Chem. C **112**, 747 (2008)
15. H. Li, Z. Bian, J. Zhu, D. Zhang, G. Li, Y. Huo, H. Li, Y. Lu, J. Am. Chem. Soc. **129**, 8406 (2007)
16. X.F. Song, L. Gao, Langmuir **23**, 11850 (2007)
17. K. Vanheusden, W.L. Warren, C.H. Seager, D.R. Tallant, J.A. Voigt, B.E. Gnade, J. Appl. Phys. **79**, 7983 (1996)
18. J. Li, L.J. Cai, J. Shang, Y. Yu, L.Z. Zhang, Adv. Mater. **28**, 4059 (2016)
19. G.H. Dong, Z.H. Ai, L.Z. Zhang, RSC Adv. **4**, 5553 (2014)
20. A.I. Kontos, V. Likodimos, T. Stergiopoulos, D.S. Tsoukleris, P. Falaras, I. Rabias, G. Papavassiliou, D. Kim, J. Kunze, P. Schmuki, Chem. Mater. **21**, 662 (2009)
21. J. Jiang, L.Z. Zhang, H. Li, W.W. He, J.J. Yin, Nanoscale. **5**, 10573 (2013)
22. H. Li, L.Z. Zhang, Nanoscale. **6**, 7805 (2014)
23. H. Li, J.G. Shi, K. Zhao, L.Z. Zhang, Nanoscale. **6**, 14168 (2014)
24. G.H. Dong, L.Z. Zhang, J. Mater. Chem. **22**, 1160 (2012)
25. G.H. Dong, K. Zhao, L.Z. Zhang, Chem. Commun. **48**, 6178 (2012)
26. X.C. Meng, L.Y. Jiang, W.W. Wang, Z.S. Zhang, Int. J. Photoenergy **2015**, 747024 (2015)
27. H. Li, J. Shang, J.G. Shi, K. Zhao, L.Z. Zhang, Nanoscale. **8**, 1986 (2016)
28. J.L. Wang, Y. Yu, L.Z. Zhang, Appl. Catal. B Environ. **136–137**, 112 (2013)
29. Y.J. Gu, M.Y. Xing, J.L. Zhang, Appl. Surf. Sci. **319**, 8 (2014)
30. W.Z. Fang, M.Y. Xing, J.L. Zhang, Appl. Catal. B Environ. **160–161**, 240 (2014)
31. J. Li, L.Z. Zhang, Y.J. Li, Y. Yu, Nanoscale. **6**, 167 (2014)
32. J. Jiang, X. Zhang, P.B. Sun, L.Z. Zhang, J. Phys. Chem. C **115**, 20555 (2011)
33. H. Xu, L.Z. Zhang, J. Phys. Chem. C **114**, 11534 (2010)
34. Y.N. Wang, K.J. Deng, L.Z. Zhang, J. Phys. Chem. C **115**, 14300 (2011)
35. X. Zhang, L.Z. Zhang, T.F. Xie, D.J. Wang, J. Phys. Chem. C **113**, 7371 (2009)
36. S.X. Ge, L.Z. Zhang, Environ. Sci. Technol. **45**, 3027 (2011)
37. H. Xu, L.Z. Zhang, J. Phys. Chem. C **113**, 1785 (2009)
38. H. Xu, L.Z. Zhang, J. Phys. Chem. C **114**, 940 (2010)
39. Y.W. Wang, L.Z. Zhang, S. Li, P. Jena, J. Phys. Chem. C **113**, 9210 (2009)
40. X. Zhang, L.Z. Zhang, J. Phys. Chem. C **114**, 18198 (2010)
41. J. Jiang, H. Li, L.Z. Zhang, Chem. Eur. J. **18**, 6360 (2012)
42. J. Jiang, L.Z. Zhang, Chem. Eur. J. **17**, 3710 (2011)
43. S. Sajjad, S.A.K. Leghari, F. Chen, J.L. Zhang, Chem. Eur. J. **16**, 13795 (2010)
44. Y.L. Zhang, Z.F. Yin, C.M. Dai, X.F. Zhou, W. Chen, J. Colloid Interface Sci. **481**, 210 (2016)
45. Y.L. Zhang, C.M. Zhang, X.F. Zhou, Z. Shen, F.C. Zhao, J.F. Zhao, J. Environ. Sci. **46**, 174 (2016)
46. Y.J. Qian, X. Guo, Y.L. Zhang, Y. Peng, P.Z. Sun, C.H. Huang, J.F. Niu, X.F. Zhou, J.C. Crittenden, Environ. Sci. Technol. **50**, 772 (2016)
47. Y.N. Huo, J. Zhang, M. Miao, Y. Jin, App. Catal. B: Environ. **111–112**, 334–341 (2012)
48. Y.F. Yang, F. Zhou, S. Zhan, Y.J. Liu, Y.F. Yin, J. Inorg. Organomet. Polym. **26**, 91 (2016)
49. J. Jiang, L.Z. Zhang, H. Li, W.W. He, J.J. Yin, Nanoscale. **5**, 10573 (2013)
50. J.L. Zhang, L.S. Zhang, X.F. Shen, P.F. Xu, J.S. Liu, CrystEngComm **18**, 3856 (2016)
51. S.J. Zhang, D.Y. Wang, RSC Adv. **5**, 93032 (2015)
52. S.S. Yi, F. Zhao, X.Z. Yue, D.J. Wang, Y.H. Lin, New J. Chem. **39**, 6659 (2015)
53. H.P. Jiao, X. Yu, Z.Q. Liu, P.Y. Kuang, Y.M. Zhang, RSC Adv. **5**, 16239 (2015)
54. D. Zhang, J. Li, Q.G. Wang, Q.S. Wu, J. Mater. Chem. A. **1**, 8622 (2013)